This document is confidential and is proprietary to the American Chemical Society and its authors. Do not copy or disclose without written permission. If you have received this item in error, notify the sender and delete all copies.

Deciphering the distribution and speciation of arsenic, lead, silica, phosphorous, tin and zinc in a porous ferrihydrite grain using Transmission Electron Microscopy and Atom Probe Tomography

Journal:	*ACS Earth and Space Chemistry*
Manuscript ID	Draft
Manuscript Type:	Article
Date Submitted by the Author:	n/a
Complete List of Authors:	Schindler, Michael; Laurentian University, Earth Sciences Schreckenbach, Max; University of Manitoba, Department of Earth Sciences Wirth, Mark; Environmental Molecular Sciences Laboratory Qafoku, Odeta; Pacific Northwest National Laboratory, Environmental Molecular Sciences Laboratory Kovarik, Libor; Environmental Molecular Sciences Laboratory Perea, Daniel; Pacific Northwest National Laboratory, Environmental Molecular Sciences Laboratory

SCHOLARONE™
Manuscripts

Deciphering the distribution and speciation of arsenic, lead, silica, phosphorous, tin and zinc in a porous ferrihydrite grain using Transmission Electron Microscopy and Atom Probe Tomography

Michael Schindler[1], Max Schreckenbach[1], Mark G. Wirth[2], Odeta Qafoku[2], Libor Kovarik[3] ,

Daniel E. Perrera[2]

.

1 Department of Earth Sciences, University of Manitoba, Winnipeg, MB R3T 2N2, Canada

2 Environmental Molecular Sciences Laboratory (EMSL), Pacific Northwest National Laboratory, Richland, WA 99354, USA

3 Physical and Computational Sciences Directorate, Pacific Northwest National Laboratory, Richland, WA 99354, USA

KEYWORDS Atom Probe Tomography, Transmission Electron Microscopy, Ferrihydrite, Porosity, Arsenic, Lead, Phosphate, Silica

ABSTRACT

The interaction of contaminants and nutrients with soil constituents is controlled by processes in intergranular and intragranular pore spaces of organic matter or/and common secondary minerals such as ferrihydrite, $Fe^{3+}_{10}O_{14}(OH)_2$. This contribution shows that the distribution and speciation of the contaminants As, P, Pb, Si, Sn and Zn in a porous ferrihydrite grain is greatly affected by the heterogeneous pore size distribution as well as the ability of the elements to polymerize. TEM and APT studies are conducted on Focused Ion Beam (FIB) sections extracted from a porous ferrihydrite grain from the smelter-impacted top soils in Sudbury, Ontario, Canada. The ferrihydrite grain has pore spaces ranging in diameter from tenths to hundreds of nanometers. TEM and Scanning-TEM studies indicate that the surfaces of the pore walls are enriched in Si and that in contrast to P, the elements As, Pb, Sn and Zn are heterogeneously distributed within or on the surface of the pore walls. APT confirms the clustering of As, Pb, Sn and Zn and suggests the

occurrence of polymerized ($As^{3+}O_x$) and ($Pb^{2+}O_x$) polyhedra. Speciation and distribution of Si, As, Pb, Sn and Zn implies that sequestration processes of these elements in porous constituents within a soil environment is affected by adsorption, desorption, diffusion, polymerization and nucleation processes. Understanding these processes in soil environments requires multi-analytical approaches and in this regard advantages and disadvantages of the combination TEM and APT to characterize complex environmental samples at the atomic- to nanometer scale are discussed.

1.0 Introduction

Iron-(hydr)oxides such as hematite, maghemite, magnetite, goethite, akaganeite, lepidocrocite, feroxyhyte, ferrihydrite, hydrohematite play fundamental roles in biogeochemical processes at the Earth's surface due to their wide occurrence and high reactivity[1, 2] An important member of this mineral group is ferrihydrite ($Fe^{3+}_{10}O_{14}(OH)_2$), a reddish-brown, poorly ordered Fe-(hydr)oxide

with variable and non-stoichiometric composition[1-3]. It is a nanocrystalline phase composed of individual particles or domains in the lower nanometer range [4, 5]. The mineral has a high surface-area and surface-reactivity and plays a significant role as a scavenger of trace metals and metalloids in various near-surface environments [1-3, 6]. Two competing structural models exist for ferrihydrite: one in which Fe is exclusively octahedrally coordinated, and one in which 20 % of the Fe atoms are tetrahedrally coordinated [so called akdalite model] [7, 8].

Nanoparticles (NPs) of ferrihydrite have often a low enough surface energy to occur as metastable constituents in soils [9]. Depending on its chemical composition, the composition of the pore fluids, pH, T and water activity, ferrihydrite NP's aggregate and transform over time into hematite or goethite via re-arrangement and dissolution-re-precipitation [1, 2].

Ions present during the formation of ferrihydrite either co-precipitate with the mineral or sorb onto the surfaces of NPs prior to or after their aggregation. Prior to aggregation, ferrihydrite NPs have a higher adsorption capacity (due to a larger number of adsorption sites) and the adsorption of an ion is not limited by diffusion into the aggregates or clusters [10]. The presence of adsorbed or incorporated ions such as silica, organic molecules, arsenic and phosphate can subsequently affect

the mineral's surface chemistry, reactivity, sorption properties [4, 11-17] and the aggregation rate of the NPs and their Oswald ripening [10, 12-16].

Ferrihydrite and other Fe-(hydr)oxides often form during weathering processes in soils. These processes include parent mineral dissolution and secondary mineral precipitation which can result in the complete replacement of minerals or organic material by secondary minerals such as Fe-(hydr)oxides[18]. Secondary minerals formed during dissolution-precipitation processes are often highly porous due to continuous mass fluxes between reaction fronts along earlier and later formed minerals and the bulk soil[19, 20]. Hence, precipitates of Fe-hydr(oxide) formed during the weathering of Fe-bearing minerals in soils, sediments and rock coatings are often porous and define the surface properties of the underlying mineral [19, 20].

Porous materials dominate reactive surface areas in geologic media [21], and thus play a more dominant role in limiting contaminant transport compared to minerals with well-defined surface properties and areas [20-24]. Unique chemical and physical properties of porous minerals such as limited flow potential and diffusion control solute transport between pore spaces and can affect sequestration, release and speciation of contaminants as well as the composition and type of phases

nucleating within the porous matrix. For example, Liu et al. [25] demonstrated that effective reaction rates can be orders of magnitude lower in heterogeneous porous media than those observed in well-mixed, homogeneous systems. Singer et al. [26] showed that pore-space heterogeneities control redox processes involving As^{3+} and As^{5+} species and Schindler and Hochella [27, 28] discovered that pore size heterogeneities can lead to complex mineralogical compositions with up to 11 different nano-size phases in porous mineral surface coatings.

In this special issue to honor Michael Hochella, we apply a combination of the focussed ion beam technology (FIB), transmission electron microscopy (TEM) and atom probe tomography (APT) to visualize and characterize metal(loid)-rich domains at the atomic- and nano-scale in a heterogonous porous ferrihydrite grain from the smelter-impacted soils in Sudbury, Ontario, Canada. Furthermore, we will test whether APT next neighbour analyses can provide information on the speciation of the metal(loid)s incorporated or adsorbed to the ferrihydrite grain and will subsequently discuss the limitations of this analysis. We will focus in our study on the distribution of the major impurities As, P, Pb, Si, Sn and Zn in a ferrihydrite grain and thus will shortly summarize their interaction with the latter mineral.

1.1 Arsenic, phosphorous, silica, lead, tin and zinc interaction with ferrihydrite

Arsenic: Arsenic adsorption onto Fe-(hydr)oxides such as ferrihydrite seems to be the main mechanism for controlling the fate and transport of As[29] The surface of ferrihydrite is mainly positively charged below its point of zero charge (pzc at pH = 7-8) and should favour the adsorption of the As^{5+} oxyanion, $(HAsO_4)^{2-}$, over the neutral As^{3+} oxyanion H_3AsO_3[30]. However, Qui and Pichler (2014) [31] showed that in the presence of As^{3+} and As^{5+} species, species of both ions adsorbed almost equally up to a pH of 5 and that adsorption of As^{3+} species is favoured over those of As^{5+} species at higher pH values, in accordance with other studies[30]. Adsorption of As^{5+} species on ferrihydrite occurs predominantly as inner sphere bidentate binuclear ("bridging") complexes with two adjacent edge-sharing Fe^{3+}-octahedra[32, 33]. Adsorption complexes involving As^{5+} species can convert to amorphous ferric arsenate surface precipitates with increasing amount of As on the surface[34].

Phosphorous: The long-term storage of phosphate in soils is commonly controlled by the type and amount of phosphate-bearing minerals. Phosphate ions either sorb to the surfaces of Fe-, and Al-oxides and clay minerals or precipitate as Ca-or Fe-phosphates[35]. This is also reflected in the

transport mode of P in natural waters, which occurs predominantly via adsorption complexes on mineral particles and not in the form of soluble phosphate species[10]. Similar to arsenate groups, phosphate adsorption on ferrihydrite occurs predominantly as bidentate-binuclear surface complex[36], which convert with increasing P loading to ternary surface complexes and to the precipitation of an amorphous Fe-phosphate[37].

Silica: Anions of silicic acid (H_4SiO_4) are the most common oxyanions in soil pore water and are an important impurity in ferrihydrite with implication to its stability and transformation[3]. They lower the crystallinity of the mineral and modify its morphology, magnetic ordering and solubility[12]. A decrease in crystallinity has been explained with the formation of Fe–O–Si complexes during the precipitation of ferrihydrite, which delay the nucleation and growth of ferrihydrite crystallites[38]. Adsorption complexes between silicic acid species and the ferrihydrite surface impede the crystal growth of the mineral, which consequently results in a decrease in particle size and crystallinity with increasing Si content of Si[12]. The silica-ferrihydrite interaction at low Si : Fe atomic ratios involves the adsorption of monomeric silica species, whereas polymerization of silica species to an amorphous Si-rich phase occurs at high Si : Fe ratios[14].

Lead: The chemistry of Pb in contaminated soils is complex due to its tendency to interact strongly with multiple mineral and organic phases dependent on pH, redox conditions, and other soil properties. Pb^{2+} can adsorb onto the surface of organic matter and Fe, Al, and Mn-(hydr)oxides or precipitate as secondary phases[39]. Pb^{2+} species predominantly sorb onto ferrihydrite via inner sphere monodenate and bidentate complexes[40].

Tin: The inorganic geochemistry of Sn is dominated by Sn^{2+} and Sn^{4+}, with the latter being highly immobile due to the low solubility of cassiterite (SnO_2)[41]. Interaction of Sn^{2+} with goethite and magnetite results in the oxidation of Sn^{2+} to Sn^{4+} and the formation of adsorption complexes involving Sn^{4+}-octahedra sharing edges or two corners with Fe^{3+} -octahedra[41, 42].

Zinc: In acidic soils, Zn adsorbs via outer sphere complexes on phyllosilicates and inner sphere surface complexes on Fe-oxides[43]. Adsorption complexes of Zn with ferrihydrite involve binuclear bidentate complexes whereas co-precipitation of Zn with ferrihydrite results in its polydentate complexation with Zn sharing corners with more than two adjacent edge-sharing Fe^{3+}-octahedra[44]. At higher Zn/Fe ratios, precipitation of Zn-hydroxides occurs in which Zn can be either tetrahedrally or octahedrally coordinated[44].

1.2 Atom Probe tomography

Atom-probe tomography (APT) is a microscope which is able to provide atomic-scale distribution maps of chemical species[45]. The technique is based on time-of-flight mass spectrometry and allows the detection and distribution of impurities (at the μg kg^{-1} range) in solid materials as 3D composition point cloud maps [46], [47, 48]. APT systems utilize the application of either ultra-fast voltage or laser pulses to erode atoms located at the tip of a needle-shaped specimen as positively charged ions by a process known as field evaporation. An electric field accelerates these ions towards a position-sensitive detector that registers the time-of-flight and relative impact position of each individual ion [49]. By relating the field evaporated ion kinetic energy to the potential energy of the electric field, the time-of-flight is used to determine the mass-to-charge-state ratio, allowing the recording of a mass spectrum with sufficient mass resolution to resolve every isotope in the periodic table. The relative impact positions of the point projected ions onto the position-sensitive-detector are used to reconstruct 3D composition point cloud maps of individual atoms and small molecular clusters. The distribution and identity of individual atoms and small molecular clusters can serve as a powerful tool to examine compositional heterogeneity and buried interfaces between different regions [46, 49]. The detection efficiency of the LEAP 4000-

HR used for APT in this study lies around 37% but depends on the field evaporation dynamics of the material. It is important to note that differences in the evaporation field of materials in complex heterogeneous environmental samples may lead to aberrations in the field evaporation and thus to the delocalization of atoms during the 3D reconstruction of the data.

APT has been used to characterize a wide range of geological materials including phosphates[50], carbonates [51-53], oxides [54-56], sulfides [57, 58], sulfates [59], silicates [60, 61] and diamonds [62, 63]. The combination of APT and TEM has, to our knowledge, never been applied to understand the distribution of metal(loid)s in ferrihydrite.

2.0 Methodology

Characterization of a ferrihydrite grain with TEM and APT requires the targeted extraction of micrometer-size specimens using a dual beam Focused Ion beam /Scanning Electron Microscope (FIB/SEM) commonly referred to as just FIB. This can be achieved for example through the extraction of FIB lamella from a micrometer-size aggregate of ferrihydrite NPs. We identified such an aggregate in our ongoing study on the mineralogical and chemical composition of acidic and limed surficial soils in Sudbury, Ontario, Canada.

2.1 Sampling site and background information on the Sudbury soils

In 1886, large Ni–Cu deposits were discovered in the Greater Sudbury area Ontario, Canada, and within two years open roast beds and smelters with short emission stacks were constructed to process local ore. During the peak years of emission, these smelters annually emitted (on average) ~1.5 million tonnes of SO_2, 200 tonnes of Pb, 120 tonnes of As, 50 tonnes of Se, and over 1000 tonnes of Cu and Ni[27, 64]. The emission of vast amounts of SO_2, H_2SO_4, and particulate matter via the smelting process, followed by remediation efforts, led to drastic changes in the geochemistry of soils located proximal to the smelting centers[27]. Surficial soil samples (upper 5cm) were collected circa 3.5 km south (red circle in Fig. 1a) of the smelter complex (green circle in Fig. 1b) at 46˚26`45¨N 81˚03`18¨ (Fig. 1a). The site is characterized by a relative sharp boundary between acidic soils of pH = 3.7 and remediated (limed) soils of pH = 5.7. The soil grain selected for the TEM and APT studies originated from a soil sample collected in the acidic part of the sampling site (Fig. S1, S = supplementary data).

2.2 Bulk characterization of the soil samples

The pH value of the soil samples was measured by mixing 2 g of soil with 10 mL of a 0.01 M $CaCl_2$ solution. The mixture was thoroughly stirred for 30 minutes and allowed to settle for 15 minutes before the pH measurement. Total carbon and sulfur of the soil sample were measured with the CHNS/O Analyzer Elementar VarioEL Cube at the Pacific North West National Laboratory (PNNL). The soil digestion process and inductively coupled plasma-mass spectrometry (ICP-MS) measurements of the soil were conducted at the Geo Labs, Sudbury, ON, Canada. Samples were prepared in a reverse aqua-regia digest and analyzed with an iCAP Q ICP-MS (Thermo Scientific).

X-ray diffraction (XRD) patterns were measured from 2 to 80 ˚2θ using a Panalytical X'Pert Bragg-Brentano diffractometer with Cu-Kα radiation (λ = 1.5418 Å), a graphite post-diffraction monochromator, and variable divergence and anti-scatter slits (illuminated length= 10 mm) at PNNL. The 2θ axis was scanned at 0.6 ˚/min and data collected at 0.04 ˚2θ intervals. Minerals were identified through comparison with reference patterns in the ICDD database (International Center for Diffraction Data, PA) using JADE (Materials Data Inc., CA; Fig. S1, S = supplementary data).

2.3 Structural and compositional characterization of the soil sample at the micro-, nano- and atomic scale

Soil samples from the acidic and limed parts were embedded into epoxy pucks, polished and subsequently characterized with an environmental field emission scanning electron microscope (FEI Quanta 650 FEG Environmental SEM) at the Manitoba Institute of Materials (MIM) at the University of Manitoba. The SEM was operated with an accelerating voltage of 20 kV and a beam current of 1 nA.

One FIB section for TEM (FIB-TEM section) and one for APT (FIB-APT) sections were extracted from the selected ferrihydrite grain (Fig. 1c and d) by lift-out technique (Ga ions) with a FEI Helios 600 NanoLab FIB at PNNL, USA. (Fig 1c). For quality control purposes, the FIB-TEM was pre-characterized at PNNL using a Titan 80-300 scanning transmission electron microscope (STEM) followed by a more thorough characterization of the FIB-TEM section was conducted with a field emission TEM FEI Talos F200x at the MIM. APT analysis was conducted at PNNL with a LEAP® 4000 XHR Local Electrode Atom Probe (LEAP) tomography instrument. APT

measurements were conducted in laser mode with a UV laser (λ = 355 nm), a pulse rate of 100-200 kHz, ion detection rate of 0.002 ions/pulse, and a pulse energy range of 5-25 pJ.

The APT data was processed using the IVAS v3.6.18 and v3.8.8 software packages. The mass spectra of all APT datasets are complex due to the formation of metal(loid)-bearing species with different charge states. Hence, visualization of metal(loid)s at the atomic level with APT is not straightforward and requires interpolation of data. Some atomic species are represented by multiple peaks or by peaks corresponding to complex-ions. As a result, peaks corresponding to species of different atomic identities and charge-to-mass ratios overlap. For example, Fe and Si produce several overlapping peaks in the mass to charge ratio vs counts spectrum. Hence, only characteristic isotopic peaks for both Fe ($^{54}Fe^{+}$: 53.9, $^{56}Fe^{+}$: 55.8, $^{57}Fe^{+}$: 56.9 Da) and Si ($^{30}Si^{+}$: 29.1 Da) were used to generate their distribution plots as otherwise differences in their locations in the 3D space could not be resolved (Fig. S4). The identified locations of the atomic species are shown in this study in the form of 2D spatial maps composition heat representing their density (ions per nm^3) and in the 3D space as spheres with radii corresponding to the sum of radii between the metal(loid) and the O-atom. These ionic radii are 0.14 nm for O^{2-}, 0.0535 nm for $^{[6]}Al$, 0.058

nm for $^{[6]}As^{3+}$, 0.058 nm for $^{[4]}As^{5+}$, 0.0335 nm for $^{[6]}Fe^{3+}$, 0.026 nm for $^{[4]}Si^{4+}$, 0.017 nm for $^{[4]}P^{5+}$, 0.119 nm for $^{[6]}Pb^{2+}$, 0.069 for $^{[6]}Sn^{4+}$, 0.06 for $^{[4]}Zn^{2+}$ and 0.074 for $^{[6]}Zn^{2+}$ [65].

Insights into clustering and speciation of As, P, Pb, Si, Sn and Zn in the APT-FIB was analyzed with a first nearest neighbor analysis (1NN)[66]. The 1NN analysis includes the experimental (actual) distribution of the ions, which is then compared to their randomized (averaged) distribution[66 67, 68]. A chi-square statistical test is used to quantitatively confirm or reject deviation from randomness. For a chi-square (χ) statistical test, the null hypothesis is that the experimental distribution is consistent with the expected random distribution (on the basis of the degrees of freedom and a 95% confidence). Large differences between the experimental (observed) χ^2 values and expected χ^2 values reject the null hypothesis and indicate that the experimental 1NN distribution of an ion is non-random; i.e. the ion is concentrated in clusters or along interfaces[66, 69].

3.0 Results

The collected soil sample has the typical mineralogical composition of an acidic soil in the Sudbury area with quartz as the major phase and albite, microcline and clinochlore as minor phases (Fig.

S1)[70]. The soil sample contains elevated concentrations of Cu and Ni (Table 1), also characteristic for the soils in the Sudbury area[71].

Semi-quantitative analyses using energy dispersive spectroscopy (EDS) with SEM (SEM-EDS) SEM-EDS and in scanning-TEM mode (STEM) indicate that the selected ferrihydrite grain and the FIB-TEM section are enriched in P, S, As, Sn, Zn and Pb relative to the bulk soil and that their Cu- and Ni-concentrations are below the detection limit of the EDS system (~1000 $mgkg^{-1}$; Table 1). SEM-EDS analyses (Table 1) and chemical distribution maps (Fig. 1d, S2) also show that Pb, As, Sn and Zn are more heterogeneous distributed than Si and P in the ferrihydrite grain at the micrometer scale.

STEM imaging of the FIB-TEM section indicates the occurrence of a highly porous matrix within the ferrihydrite grain (Fig. 2a, Fig. S2). The pore sizes vary between tenths to hundreds of nanometers and are surrounded by irregular shaped pore walls (Fig. 2a, b and S2). In thinner parts of the FIB-TEM section, STEM-EDS chemical distribution maps indicate that the outer surfaces of the pore walls are enriched in Si relative to their interior (Fig. 2c and S2). Visualization of the distribution of minor elements at the nano-scale is not trivial, especially if their major EDS peaks

overlap. This is commonly the case for S, Pb and As, as their X-ray energies S Kα and Pb Mα overlap at 2.3 keV and As Kα and Pb Lα at 10.5 keV. Hence, the best visualization of the differences between the chemical distribution of Pb and As versus P were obtained using the EDS energies of 10.5 keV for Pb + As and 2.0 keV for P Kα. The corresponding chemical distribution map suggests that P (yellow) is more homogeneously distributed relative to Pb and As (blue) (Fig. 2d). Similarly, STEM-EDS distribution maps indicate that Zn is more homogeneously distributed than Sn (Fig. S2)

The Fe-(hydr)oxide matrix is composed of nano-domains with diameters varying between 4 and 20 nm (Fig. 2e), which are larger than those observed in previous studies (<5 m][5, 12]. The domains depict lattice fringes with d = 2.0 Å (103) in similar orientations, which is also apparent in a Fast Fourier Transformation pattern (Fig. 2e) Selected area diffraction (SAED) pattern (Fig. S3) indicate sharp diffraction spots with d = 2.0 Å (103) (110) and diffuse diffraction ring at d = 2.5 Å and d = 1.47 Å. Size of the domains, the similar orientation of their lattice fringes and the occurrence of sharp diffraction spots and diffuse rings in the SAED pattern indicate that the grain is composed of a mixture of ferrihydrite and a crystalline (unknown) Fe-(hydr)oxide.

3.1 Distribution of the elements at the atomic to nano-scale

Embedding the soil sample in epoxy resulted in the closure of the majority of pores in the ferrihydrite grain. This increased the physical stability of the grain and allowed the extraction of the FIB-TEM and FIB-APT sections. Consequently, the extracted FIB-APT contains pore spaces filled with epoxy and these areas can be recognized in a 2D chemical distribution map for Fe (xz-plane) as Fe-depleted areas (Fig. 4a). Hence, areas in the ferrihydrite grain depleted or enriched in the elements As, Pb, Si, P, Sn and Zn can be only recognized when comparing their 2D chemical distribution maps with the one for Fe (Figs. 4-5, S5-S7). Areas in ferrihydrite enriched in As, P, Pb, Si, Sn and Zn are indicated with red and white rectangles and circles in the corresponding 2D chemical distribution maps. These areas occur as nanometer-size domains with diameters in the 5 to 10 nm range.

Domains enriched in As and P occur in higher number in the upper part of the FIB-APT (Figs. 3b-c), those enriched in Pb are concentrated in the lower part (Fig. 3d) and domains enriched in Si, Zn and Sn are relatively homogeneously distributed Fig. (4a, S6 and S7). Here, domains enriched in Si depict a unique feature as they sandwich a domain of ferrihydrite (Fig. 4a).

In crystal chemistry, the polymerization or clustering of cations and anions is commonly depicted with either ball-stick models or with polyhedra, whereby polyhedral representations are used often to depict the location and connectivity of cation-centered polyhedra. As the set of O-atoms is incomplete in an APT dataset, cation-centered polyhedra for $As^{3+/5+}$, Si^{4+}, P^{5+}, Pb^{2+}, Sn^{4+} and Zn^{2+} are depicted as spheres with radii corresponding to the sum of radii for the cation and the O-atom. For example, Figure 4b depicts a 3D plot of Fe-octahedra and silica polyhedra, represented by spheres with radii of 0.2 (sum of the radii for $^{[6]}Fe^{3+}$ and O^{2-}) and 0.17nm (sum of the radii for $^{[4]}Si^{4+}$ and O^{2-}), respectively (Fig. 4b). This plot indicates similar to the 2D plot (Fig. 4a), the occurrence of silica-rich domains around a domain of ferrihydrite.

1NN analyses for As, P, Pb, Si, Sn and Zn were calculated for the entire sample as well as for domains enriched in these elements (labelled with red rectangles in Figs. 3-4 and numbered from 1 to 6, plots of the 1NN analysis for P, Sn and Zn are shown in Fig. S5-S7). As the entire sample includes also pores filled with epoxy, none of the elements can occur in a complete random fashion and their corresponding observed χ^2 are thus greater than the expected χ^2 values (Table 2). Comparison between the observed and expected χ^2 values for As, Pb, Sn, Zn, Si and P indicates that (a) the first three elements display a higher degree of clustering (i.e. are less random

distributed) than the latter three elements and (b) the distribution of P depicts the lowest degree of clustering relative to the other five elements (Table 2).

1NN analyses of domains enriched in As, Pb, Si, P, Sn and Zn were carried out to identify whether observed As-As, Pb-Pb, Si-Si, P-P, Sn-Sn and Zn-Zn 1NN distances indicate (a) the polymerization of AsO_x, PbO_x, SiO_4, PO_4, SnO_x and ZnO_x polyhedra and (b) resemble those observed in the structure of simple As-, Pb-, Si-, P-, Sn-, and Zn-oxides. As the detection efficiency of APT is only 37%, elements occur in a much lower fraction in the reconstructed APT plot than in the original sample. Hence, longer As-As, Pb-Pb, Si-Si, P-P, Sn-Sn and Zn-Zn 1NN distances will be overrepresented in a 1NN analysis with respect to the actual distribution of distances in the sample.

A 3D plot of the As-rich domain 1 with As-polyhedra and Fe-octahedra represented by spheres with radii of 0.2 nm (representing the sums of the radii for $^{[6]}As^{3+}$ and O^{2-} and $^{[6]}Fe^{3+}$ and O^{2}) indicates that domains enriched in As occur within pore spaces of domains enriched in Fe^{3+}-octahedra (encircled in Fig. 5a). An APT 3D plot depicting exclusively (AsO_x) polyhedra indicates the occurrence of polymerized As-polyhedra (Fig. 5b). 1NN analysis indicates that maximum

abundances of As-As 1NN distances in this domain are in the ranges of 0.375-0.475 nm and 0.575-0.675 nm (Fig. 5c). Inspection of As-As 1NN distances in arsenite- and arsenate-bearing minerals shows that As-As 1NN distances smaller than 0.475 nm only occur in structures with polymerized ($As^{3+}Ox$) polyhedra (Fig. 5d, e). For example, in the structures of claudetite and arsenolite (As_2O_3)[72, 73], As^{3+} depicts a distorted coordination environment due to a lone-pair stereoactive electron pair. Polymerized polyhedra are bridged in both minerals either via shorter As^{3+}-O bonds trans to the electron lone pair with As^{3+}-As^{3+} 1NN distances of 0.31-0.33 nm or via shorter As^{3+}-O and longer As^{3+}---O bonds (cis to the electron lone pair) with As^{3+}-As^{3+} 1NN distances in the range of 0.35-0.45 nm (Fig. 5c). Contrary to As^{3+} polyhedra, arsenate groups do not occur as polymerized species in minerals. Short As^{5+}-As^{5+} 1NN distances occur when two arsenate tetrahedra share corners to an octahedral-coordinated smaller cation such as Fe^{3+} in cis-configuration (Fig. 5e). This is for example the case in the structure of scorodite, $FeAsO_4(H_2O)_2$ where the As^{5+}-As^{5+} 1NN distances are ~0.5 nm (Fig. 5f)[74]. Hence, the observed 1NN distances in the range of 0.375 to 0.475 nm (Fig. 5c), the touching of As-polyhedra in 3D plots (Fig. 5b) and the observed As-As distances in arsenite and arsenate minerals point towards the occurrence of polymerized arsenite groups bridged by As^{3+}-O---As^{3+} bonds. It should be noted that we could not

resolve the average valence of As with X-ray photoelectron spectroscopy (using an Ultra Axis X-ray photo spectrometer at the MIM), most likely due to the low As concentrations and the small dimensions of the ferrihydrite grain.

A 3D plot of Pb polyhedra (spheres with radii of 0.25 nm) and Fe^{3+} octahedra (spheres with a radii of 0.2 nm) for the Pb-rich domain 3 indicates the occurrence of polymerized (PbO_x) polyhedra in pore spaces of the Fe-octahedra (Fig. 6a and inlet). 1NN analysis indicates that Pb-Pb 1NN distances of 0.34-0.38 nm are the most common distances below 0.5 nm (Fig. 6b). This distance coincides with the Pb-Pb 1NN distance in Pb^{2+}-oxides such as litharge and massicot, PbO, where the edge-sharing of Pb^{2+} polyhedra results in Pb-Pb 1NN distances of ~0.36 nm[75, 76].

Visualization of the silica tetrahedra (spheres with a radius of 0.16 nm) in the Si-rich domain 5 indicates the occurrence of polymerized (SiOx) polyhedra (encircled in Fig. 5c). 1NN analysis of this domain indicates a maximum abundance of Si-Si 1NN distance of 0.45-0.55 nm. This distance is larger than the expected value for polymerized silicate tetrahedra, where Si-Si 1NN distances of ~0.31 nm occur in high and low quartz and in the range of ~0.28 to 0.34 nm[77] in amorphous silica[78].

However, a 1NN Si-Si distance of 0.45-0.55 nm occurs for example when two silica tetrahedra share corners in cis-configuration with the same Fe^{3+}-octahedron (see Fig. 5f).

A 3D plot of phosphate tetrahedra (spheres with a radii of 0.16 nm) and Fe^{3+}-octahedra (spheres with a radii of 0.2 nm) indicates the absence of polymerized phosphate groups and the presence of phosphate tetrahedra linked to Fe^{3+}-octahedra (Fig. S5). 1NN analysis of a domain enriched in P indicates that the largest number of short 1NN P-P distances (< 0.6 nm) occur in the range of 0.45-0.55 nm (Fig. S5). This range in 1NN P-P distances occurs for example when two phosphate tetrahedra, share corners in cis-configuration with the same Fe^{3+}-octahedron (as observed in strengite $Fe(PO_4)(H_2O)_2$ with d = 0.48 nm[79], see Fig. 5f).

A 3D plot for Sn polyhedra (spheres with a radius of 0.21 nm) indicates the occurrence of polymerized SnOx polyhedra in a domain enriched in Sn (Fig. S6). 1NN analysis of the latter domain shows that the highest frequency of 1NN Sn-Sn distances with d < 0.5 nm occurs between d = 0.40-0.50 nm. This range is larger than the observed range in 1NN Sn-Sn distances with d = 0.31-0.37 nm between two edge-sharing Sn polyhedra [80] but matches 1NN Sn-Sn distance of 0.47

nm which occur between chains of edge-sharing Sn-octahedra not-directly linked to each other in the structure of cassiterite [80].

A 3D atomic plot for Zn and Fe^{3+}polyhedra (spheres with radii of 0.2 nm) indicates that the majority of Zn occurs in pore spaces of the ferrihydrite rather than being incorporated into its structure (Fig. S7). 1NN analysis indicates that a large number of shorter bonds (<0.6 nm) occurs in the range of 0.375-0.425 nm (Fig. S7). Waychunas et al.[44] showed that this range of 1NN Zn-Zn distances occurs between corner-shared Zn-tetrahedra in several Zn-oxy-salt minerals.

4.0 Discussion

The acidic smelter-impacted soils in the Sudbury area are the product of the emission of vast amounts of sulfuric acid, finer particulate matter (PM < 1 μm) predominantly composed of Pb, As and S and larger PM (> 1 μm) composed of Cu-Ni-Fe-bearing spinels, silicates and sulfides[39, 70]. The release of metals from deposited PM is ongoing and occurs at a higher rate in the acidic than

limed soils[71]. The mobility of the released elements is also higher in the acidic than near-neutral soils due to the lower pH value and lack of constituents with high adsorption capacities (e.g. clay minerals and organic matter)[71]. Continuous dissolution of Fe-bearing primary soil minerals (clinochlore, micas, amphiboles, Fig. S1) and Fe-bearing particulate matter emitted from the smelter results in the release and mobilization of Fe and the precipitation of Fe^{3+}-(hydr)oxides[27, 28]. The textural features visible in the thinner parts of the FIB-TEM section (Fig. 2a) suggest that ferrihydrite replaced a porous organic substance via a dissolution-precipitation process, a process that can preserve the original texture of the replaced mineral/organic matter[19].

The enrichment of Pb, As and P in the ferrihydrite grain with respect to the bulk soil and the absence of detectable concentrations of Cu and Ni may be explained with the positive surface charge of ferrihydrite at the soil pH of pH = 3.7, the high affinity of arsenite-, arsenate, phosphate and silicic acid groups towards the surface of ferrihydrite under acidic pH conditions (see above), and the adsorption edges for Pb^{2+}, Cu^{2+} and Ni^{2+} on Fe-hydroxides with pH values of pH ~3.5 for Pb^{2+} (below the soil pH value), 4.0-4.5 for Cu^{2+} (above the soil pH value) and pH = 6.0-6.5 for Ni^{2+} (above the soil pH value)[81]. The enrichment of Zn and Sn in the ferrihydrite with respect to the bulk soil cannot be explain with the adsorption edge of Zn on ferrihydrite (pH = 5.5-6.0, above

the soil pH value)[81] and the very low concentrations of Sn^{4+}-species in soil pore solutions[41]. Similarly, adsorption processes can also not explain the heterogeneous distribution of As, Pb, Si, Sn and Zn at the micrometer (Fig. S2), nanometer (Figs. 2c, S3) and atomic (Fig. 3, 4s, S5-S7) scale and indicates that the sequestration of these elements must have been also controlled by diffusion, polymerization, nucleation and nanoparticle aggregation.

4.1 Adsorption, desorption and diffusion

The heterogeneous pore system of the ferrihydrite grain (Fig. 2a) had most likely a large effect on the transport, mixing, and interaction of Pb-, As-, Si-, Sn and Zn-bearing species within its pore system. Experimental studies and numerical studies show that effective reaction rates can (a) be orders of magnitude lower in heterogeneous porous media than those observed in well-mixed, homogeneous systems[25, 82] and (b) decrease by orders of magnitude from the molecular to macroscopic scale[82].

At the molecular scale, surface complexation is a primary process controlling metal(loid) desorption and reactive transport in sediments[82]. At the nano- to centimeter scale, metal(loid) surface complexation becomes a kinetic process, rate-limited by mass transfer in intragranular and

inter-granular domains[82]. Hence, mass transfers within the ferrihydrite grain most likely limited the supply of reactants to and the removal of reaction products from surface complexation and nucleation sites, leading to the heterogeneous distribution of As, Pb, Si, Sn and Zn. Factors that commonly control mass transfers include (a) surface roughness and composition, which control reactive surface area and reactivity and (b) heterogeneous flow and transport conditions within pores of different openings and diameter[82].

Lui et al.[25] showed that during desorption experiments involving uranyl aqueous species and a porous uranium-contaminated sediment, U concentrations were higher in smaller than larger pores and decreased faster in larger, well-connected pores than in smaller poorly connected pores. The authors explained this phenomenon with the higher solid surface to pore volume ratio in the smaller pores and their lower accessibility for advective flow. These concentration trends drove pore-scale reactive mass transfer, which affected the local dissolved uranyl concentration and its transport. Lui et al.[25] concluded that the effects of pore-scale mass transfers on the overall reaction rate increased with increasing heterogeneity of grain size, pore connectivity, and pore size distribution.

The heterogeneous pore-space distribution in the ferrihydrite grain (Fig. 2a. b and S2) and the exposure of its porous matrix to metal(loid)-bearing pore solutions over many years (perhaps even decades) suggests that adsorption, desorption, polymerization, nucleation and aggregation processes within pore spaces were strongly affected by pore-scale mass transfers. The differences in mass transfer between smaller poorly connected versus larger, well connected pore spaces in the ferrihydrite grain resulted most likely in a higher accumulation of elements or element-bearing nanoparticles in the smaller pore spaces. This conclusion is in accord with the occurrence of As-, Pb-, Si-, Sn and Zn-rich domains in the tenths of nanometer range (Figs. 3, 4, S5-S7). However, the almost homogeneous distribution of P (which occurs in similar concentrations as As-, Pb-, Sn and Zn; Table 1) in the ferrihydrite matrix indicates that a combination of adsorption and diffusion processes alone cannot explain the low abundance of phosphate-rich domains.

4.2 Polymerization and nanoparticles

STEM chemical distribution maps, APT structural plots and 1NN analyses (Fig. 2 -6) suggest the occurrence of polymerized silica, arsenite and ($Pb^{2+}O_x$) polyhedra in nano-size domains within pores of the ferrihydrite grain.

The predominant occurrence of polymerized silica species on internal surface features of the ferrihydrite (Fig. 2c) suggests either (a) adsorption and polymerization of silica species on the surfaces of pore walls and channels after the formation of the porous ferrihydrite grain or (b) accumulation and polymerization of silica species previously adsorbed to ferrihydrite NPs but then expelled during the aggregation of the NPs. The latter mechanism was proposed by Schindler et al.[5] who showed that the aggregation and Ostwald ripening of ferrihydrite NPs during the weathering of volcanic glass led to the formation of hematite and amorphous silica.

The higher degree of clustering of Pb, As, Sn and Zn relative to P, as apparent in SEM-EDS (Fig. S2) and STEM-EDS (Fig. 2 and S3) distribution maps and in the experimental X^2 values (Table 2) may be the result of (a) polymerization processes and (b) the occurrence of nanoparticles:

(a) Arsenite and ($Pb^{2+}O_x$) polyhedra are commonly distorted due to the presence of lone-pair stereoactive electrons[83]. This distortion facilitates their polymerization as

individual As^{3+}-O and Pb^{2+}-O bonds do not have commonly a bond valence of >1 vu and the resulting bond valence sum around a two-coordinated bridging O atom between two arsenite or (PbO_x) polyhedra will not exceed 2 vu (Paulings 2nd rule)[83]. Similarly, Zn-tetrahedra and octahedra polymerize on the surface of ferrihydrite at higher Zn/Fe ratios[44]. Conversely, the inability of phosphate groups to polymerize (there are only a few minerals containing diphosphate groups[84]) and their strong affinity towards Fe^{3+}-surface sites under acidic conditions[11] may have prevented their accumulation in smaller poorly connected pores and their removal from larger well-connected pores, respectively.

(b) Nanoparticles of anglesite and those containing high-field strength elements such as Ti (anatase, TiO_2) and Zr (baddeleyite, ZrO_2) have been identified in porous mineral surface coatings of smelter-impacted acidic soils[28, 85]. As TEM and APT could not provide conclusive evidence for the occurrence or absence of NPs, nucleation or aggregation of Pb-, As- and Sn-bearing NPs in the pore spaces of ferrihydrite cannot be ruled out.

To conclude, the higher degree of clustering of As, Pb, Sn, Si and Zn relative to P was most likely a product of adsorption and desorption processes (which resulted in the removal of As, Pb and Zn from larger pore spaces), precipitation and segregation processes (which resulted in the formation of the Si-enriched domains), and diffusion, polymerization and nanoparticle aggregation processes (which led to the accumulation of As, Pb, Sn and Zn in smaller pore spaces).

4.3 Microaerophilic conditions in confined pore spaces

The accumulation of most likely arsenite species in nano-size pore spaces of the ferrihydrite grain indicates the occurrence of microaerophilic conditions within the domains. This observation is in accord with the studies by Singer et al.[26] who showed that microaerophilic conditions in pore spaces can prevent the oxidation of As^{3+} in the interior of Fe-rich mineral surface coatings in sediments from Cape Cod (Massachusetts, USA). Similarly, Schindler and Hochella[27] and Mantha et al. [86] identified minerals in porous mineral surface coatings and organic matter, which are not in equilibrium with the oxidizing conditions in the surrounding surficial soils. These include for example, fougèrite or green rust, $[Fe^{2+}_{6(1-x)}Fe^{3+}_{6x}O_{12}H_{14-x}CO_3](H_2O)_3$ and covellite CuS which commonly form under reducing conditions.

4.4 Characterising environmental samples with the combination of APT and TEM

The combination of TEM and APT has as every other analytical approach advantages and disadvantages:

Advantages: The combination of both analytical techniques is complimentary as TEM provides a better overview of textural features and chemical features of interfaces such as the occurrence of surfaces enriched in Si. Although STEM-EDS chemical distribution maps suggested the clustering of Pb, As and Sn, only APT and associated 1NN analyses provided evidence for their enrichment and polymerization in nano-size domains. 1NN distance analyses could also show that many 1NN distances observed in domains enriched in As, Pb, Sn, Zn, Si and P are similar to those observed in the structures of minerals.

Disadvantages: Although STEM-EDS mapping have been improved through the development of new EDS detectors[87], the technique still lacks resolution when recording the distribution of minor elements at the nano-scale. The two major well known disadvantages of APT are the peak overlap between species in an APT spectrum and the low detection efficiency[69]. Omission of peaks containing components of different atomic identities and mass to charge state ratios (as done in

this study) and the low detection efficiency results in incomplete sets of atoms in the reconstructed APT data set. In the case of our study, an incomplete APT data set did not allow the unequivocal identification of As-, Pb-, Si- and Sn-bearing nanoparticles.

In conclusion, we believe that the combination of TEM and APT has lots of potentials, especially with the improvement of the detection efficiency of the APT. An increase in the latter efficiency will allow a better structural characterization of impurities in minerals and porous media. This knowledge will subsequently provide a better understanding on the effects of pore sizes and pore wall chemistries on the adsorption, polymerization and nucleation of contaminants.

5.0 Conclusions

The combination of TEM and APT resolved the distribution of the elements As, P, Pb, Si, Sn and Zn in a porous ferrihydrite grain from a smelter-impacted soil. This analytical approach also provided some details on the speciation of these elements in pore spaces of the ferrihydrite grain. The heterogeneous pore-size distribution in the ferrihydrite grain, adsorption, desorption and diffusion processes, the ability of As-, Pb-, Si-, Sn- and Zn- polyhedra to polymerize and the potential nucleation and aggregation of nanoparticles led to the clustering of these elements within

the porous ferrihydrite grain. Conversely, the high affinity of phosphate ions towards Fe-oxide surface terminations under acidic conditions and the inability of the phosphate ions to polymerize resulted most likely in its more homogeneous distribution in the ferrihydrite pore matrix. This study showed that the combination of TEM and APT could partially resolve the speciation of contaminants in intragranular pore spaces but failed to identify the potential occurrence of nanoparticles. We recommend that spectroscopic analytical techniques such as such as X-ray photoelectron spectroscopy and X-ray absorption spectroscopy should be added to the combination of TEM and APT. This would allow a better resolution of the degree of polymerization of e.g. the silicate tetrahedra or the average valence of elements such as As^{3+}/As^{5+}.

Acknowledgment

MS thanks Michael Hochella for his mentorship and collaborative research over the last 10 years. This project was supported by the EMSL project #50176 and a NSERC discovery grant. A portion of the research was performed at EMSL (grid.436923.9), a DOE Office of Science User Facility sponsored by the Biological and Environmental Research program. The Pacific Northwest

National Laboratory is a multi-program national laboratory operated by Battelle for the DOE under Contract DE-AC05-76RL01830.

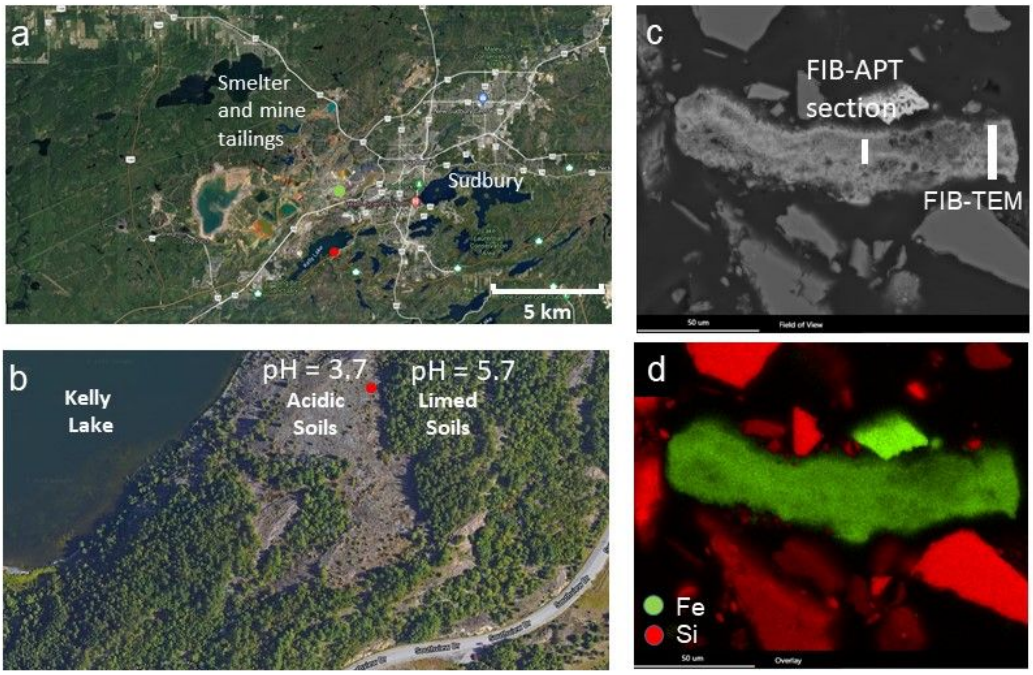

Figure 1. (a) Google satellite overview image of the Sudbury area, North-Eastern Ontario, Canada; the locations of the smelter complex and the sampling area are labelled with green and

red circles; respectively; (b) Google satellite image of the sampling site (red sphere), indicating a sharp boundary between acidic and remediated (limed) surficial soils with contact pH values of 3.7 and 5.7, respectively; (c) SEM-BSE and (d) SEM-EDS chemical distribution maps for Fe (green) and Si (red) of the selected porous ferrihydrite grain; the locations of the extracted FIB lamellae for APT and TEM are indicated.

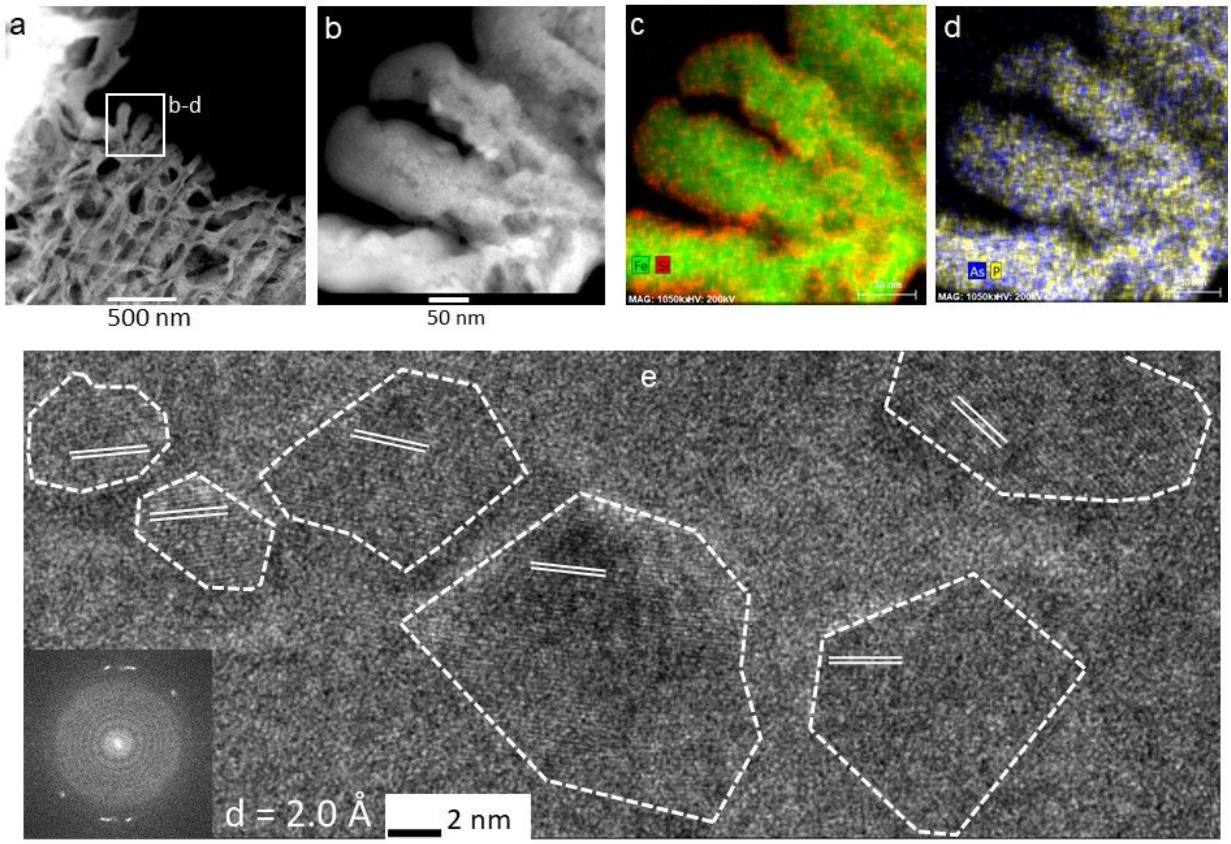

Figure 2. (a) STEM overview image of an electro-transparent part of the FIB section indicating pore spaces with diameters ranging from the tenths to hundreds of nanometers; (b) STEM images and (c)-(d) EDS chemical distributions maps for (c) Si (red) and Fe (green) and (d) Pb + As (10.5 kV, blue) and P (yellow); (e) high-resolution TEM image of an area depicted in (b) indicating nano-size domains of ferrihydrite with d-spacing of d = 2.0 Å (103).

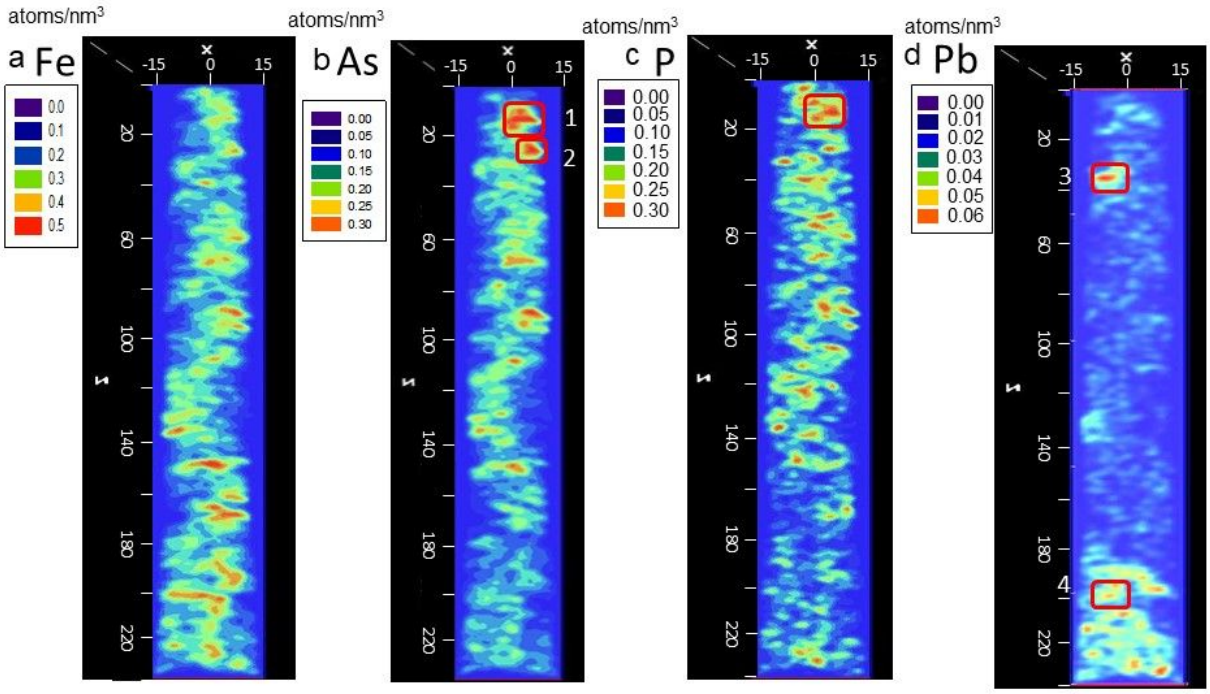

Figure 3. (a)-(d) APT 2D-chemical distribution maps for (a) Fe, (b) As, (c) P and (d) Pb; domains labelled with red rectangles (labelled 1 to 4) were further examined with 1NN distance analyses.

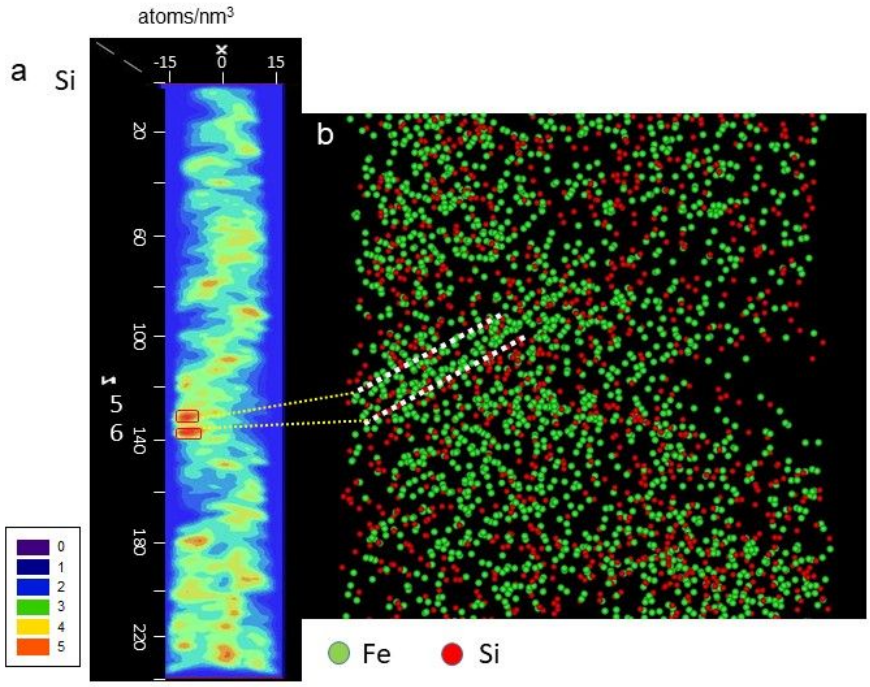

Figure 4. APT 2D-chemical distribution maps for Si, domains labelled with red rectangles (labelled 5 to 6) were further examined with 1NN distance analyses; (b) APT 3D atomic model depicting Fe-octahedra (green) and silica tetrahedra (red) as spheres with radii of 0.2 and 0.17nm, respectively; a layer of Fe octahedra (indicated with white dashed) is sandwiched by domains enriched in silica tetrahedra, corresponding to the Si-rich domains 5 and 6 indicated in (a).

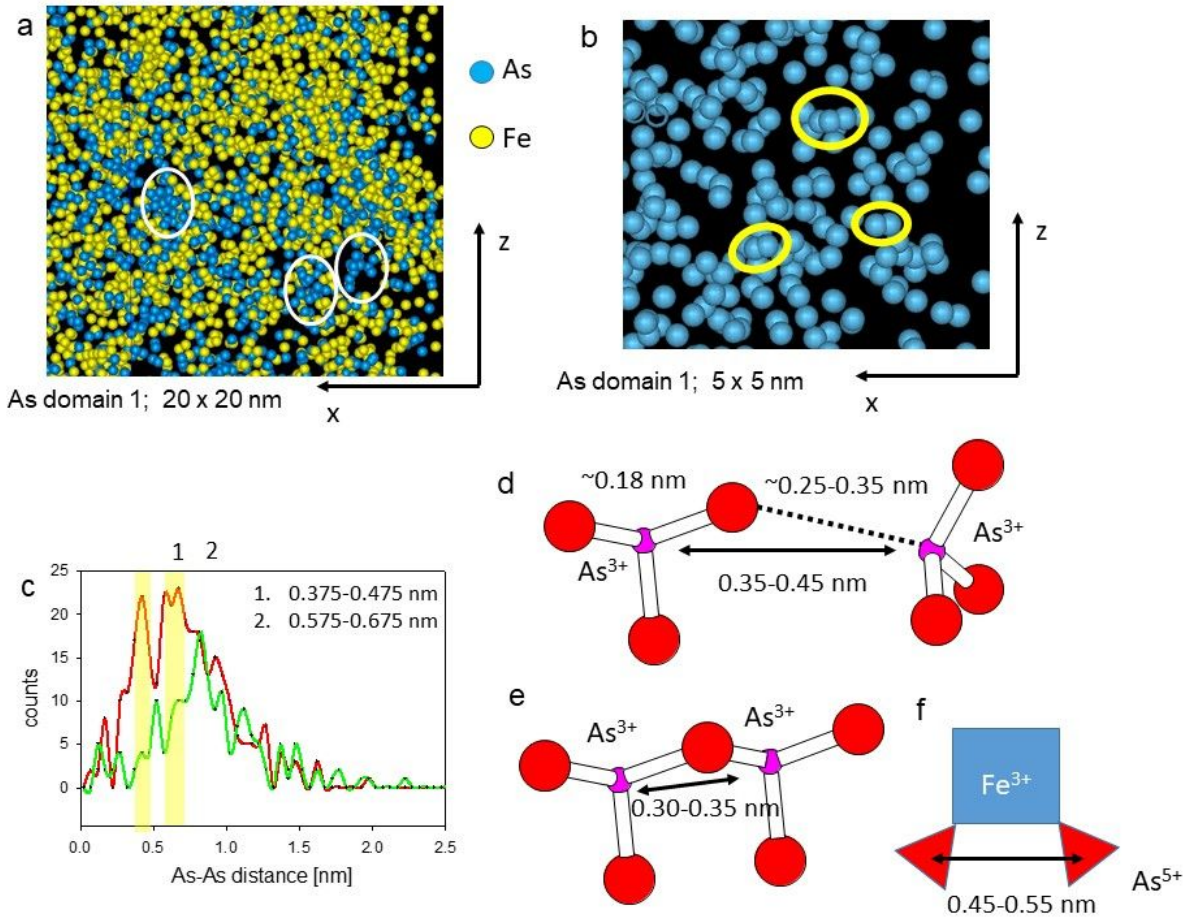

Figure 5. (a)-(b) APT 3D atomic plots for (AsO_x) polyhedra (blue) and Fe^{3+}-octahdera (yellow) in domain 1 (indicated in Figure 3b); the polyhedra are depicted as circles; occurrences of (a)

pore spaces enriched in (AsO_x) polyhedra and (b) polymerized (AsO_x) polyhedra are encircled; (c) 1NN As-As distance analyses for domain 1; the red and green line indicate the number of observed and random (averaged) 1NN As-As distances, respectively; maxima in the abundance of 1NN distances occur at 0.375-0.475 nm and 0.575-0.675 nm and are labelled with yellow bars; (d) and (e) observed 1NN As distances in the As_2O_3 polymorphs depicted with ball and stick models (As: small pink spheres; O atoms: large red spheres; (e) Fe octahedra (blue) linked to two arsenate polyhedra (red) in the structure of scorodite with 1NN As^{5+}-As^{5+} distances in the range of 0.45-0.55 nm.

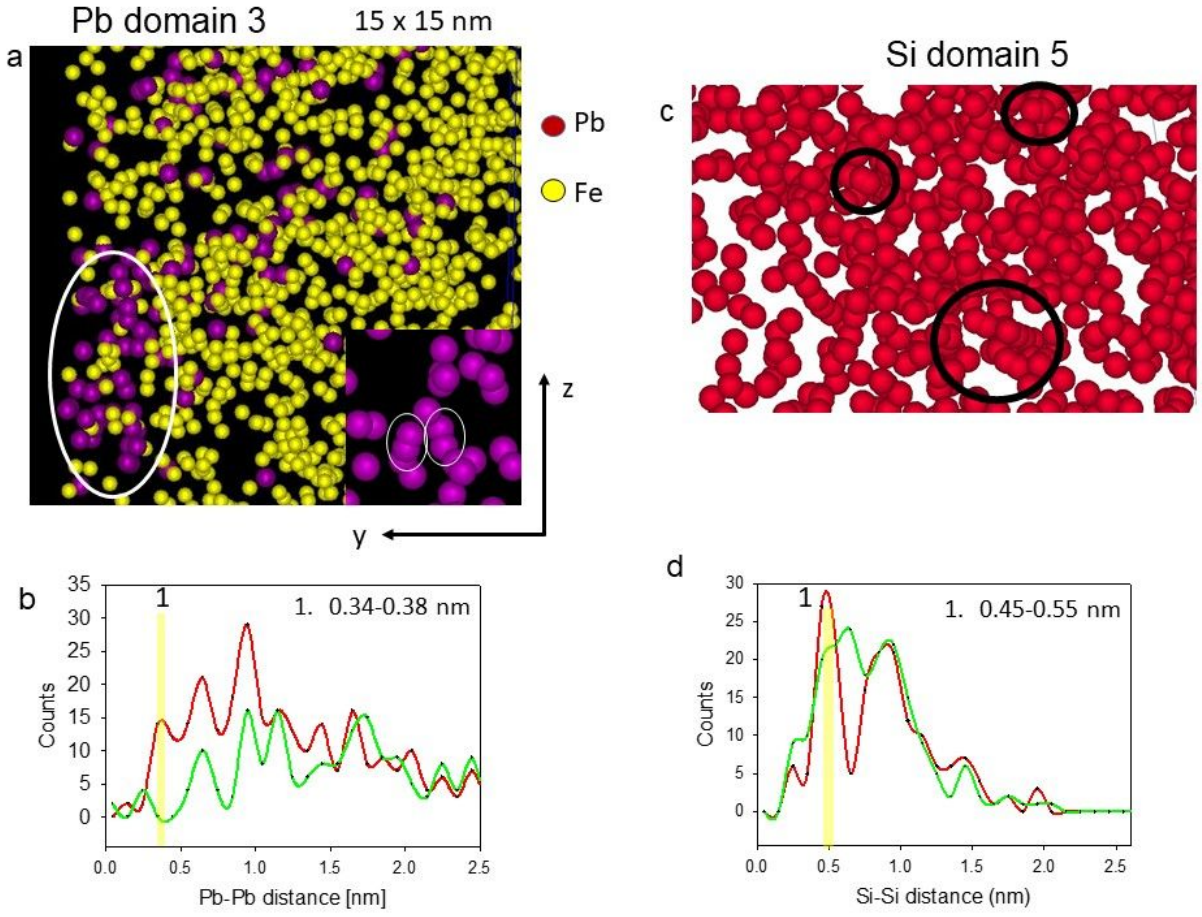
Pb domain 3
15 x 15 nm
a
Pb
Fe
z
y
Si domain 5
c
b
1
1. 0.34-0.38 nm
Counts
Pb-Pb distance [nm]
d
1
1. 0.45-0.55 nm
Counts
Si-Si distance (nm)

Figure 6. (a) APT 3D atomic plot for (PbOx) (violet) and (FeOx) (yellow) in domain 3 (indicated in Figure 3d), the polyhedra are depicted as circles; occurrences of pore spaces enriched in (PbOx) polyhedra and (inlet) polymerized (PbOx) polyhedral are encircled; (b) analyses for 1NN Pb-Pb distances in domain 1; the red and green line indicate the number of observed and random (averaged) 1NN Pb-Pb distances, respectively; an large abundance of distances below 0.5 nm occurs at 0.34-0.38 nm is labelled with a yellow bar; (c) APT 3D atomic plot of the silica tetrahedra in domain 5 (indicated in Figure 4a), the polyhedra are depicted as spheres; polymerized silica tetrahedral are encircled; (d) analyses for 1NN Si-Si distances in domain 5; the red and green line indicate the number of observed and random (averaged) 1NN Si-Si distances, respectively; a maximum in abundance of 1NN distances occurs at 0.45-0.55 nm is labelled with a yellow bar.

Table 1. Concentrations of selected elements in the collected soil sample and in the ferrihydrite grain

	Soil, pH =3.7	Grain (n= 4; SEM-EDS area analyses)	FIB section (STEM-EDS area analysis)
	[wt%]	[wt%]	[wt%]
O	n.a	31	30
Al	4.87	0.3(1)	0.3
Fe	4.45	55(2)	55.7
P	0.49	1.95(7)	2.1
S	0.10	0.46(8)	0.7
Si	32.30	0.16(7)	0.6
TOC	8.02	n.a,	n.a
	[$mgkg^{-1}$]	[wt%]	
As	177	0.71(8)	1.5
Cu	2620	Bdl	Bdl
Ni	1931	Bdl	Bdl

Pb	229	1.9(3)	1.7
Sn	7	1.2(2)	3.6
Ti	n.d	0.3(2)	0.4
Zn	70	1.8(2)	2.0

n.d. = not determined; n.a = not applied as embedded into epoxy; bdl = below detection limit

Table 2 Results of 1NN analyses for the entire sample and domains enriched in As, Pb, Sn, Si, Zn and P (mode), number (#) of first neighbors with d < 2.55 nm, experimental X^2, degrees of freedom and expected X^2; the elements are ranked on the basis of their experimental X^2 in the reconstructed sample.

Mode	# of first neighbours ≤ 2.55 nm	experimental X^2	degrees of freedom	expected X^2
As in sample	22044	388	50	66

As in cluster1	313	420	29	41
As in cluster2	87	61	17	26
Pb in sample	4128	**256**	26	38
Pb in cluster3	273	178	23	34
Pb in cluster4	162	87	19	29
Sn in sample	25020	**255**	26	38
Sn in cluster*	800	55	22	34
Zn in sample	10031	**104**	29	41
Zn in cluster*	88	73	21	31
Si in sample	21992	**89**	26	38
Si in cluster5	174	38	19	30
Si in cluster6	153	55	17	26
P in sample	4261	**51**	26	38
P in cluster*	128	123	21	31

*plots are shown in supplementary data

References

1. Cornell, R. M.; Schwertmann, U., In *The Iron Oxides*, 2003; pp 1-664.

2. Guo, H.; Barnard, A. S., Naturally occurring iron oxide nanoparticles: morphology, surface chemistry and environmental stability. *Journal of Materials Chemistry A* **2013,** *1* (1), 27-42.

3. Jambor, J. L.; Dutrizac, J. E., Occurrence and Constitution of Natural and Synthetic Ferrihydrite, a Widespread Iron Oxyhydroxide. *Chemical Reviews* **1998,** *98* (7), 2549-2586.

4. Cismasu, A.; Michel, F.; Stebbins, J.; E, B., Properties of impurity-bearing ferrihydrite I. Effects of Al content and precipitation rate on the structure of 2-line ferrihydrite. *Geochimica Et Cosmochimica Acta - GEOCHIM COSMOCHIM ACTA* **2012,** *92*.

5. Schindler, M.; Michel, S.; Batcheldor, D.; Hochella, M. F., A nanoscale study of the formation of Fe-(hydr)oxides in a volcanic regolith: Implications for the understanding of soil forming processes on Earth and Mars. *Geochimica et Cosmochimica Acta* **2019,** *264*, 43-66.

6. Waychunas, G. A.; Kim, C. S.; Banfield, J. F., Nanoparticulate Iron Oxide Minerals in Soils and Sediments: Unique Properties and Contaminant Scavenging Mechanisms. *Journal of Nanoparticle Research* **2005,** *7* (4), 409-433.

7. Michel, F.; Ehm, L.; Antao, S.; Lee, P.; Chupas, P.; Liu, G.; Strongin, D.; Schoonen, M.; Phillips, B.; Parise, J., The Structure of Ferrihydrite, a Nanocrystalline Material. *Science (New York, N.Y.)* **2007,** *316*, 1726-9.

8. Michel, F. M.; Barrón, V.; Torrent, J.; Morales, M. P.; Serna, C. J.; Boily, J.-F.; Liu, Q.; Ambrosini, A.; Cismasu, A. C.; Brown, G. E., Ordered ferrimagnetic form of ferrihydrite reveals links among structure, composition, and magnetism. *Proceedings of the National Academy of Sciences* **2010,** *107* (7), 2787.

9. Navrotsky, A., Thermochemistry of Nanomaterials. *Reviews in Mineralogy & Geochemistry - REV MINERAL GEOCHEM* **2001,** *44*, 73-103.

10. Paige, C. R.; Snodgrass, W. J.; Nicholson, R. V.; Scharer, J. M.; He, Q. H., The effect of phosphate on the transformation of ferrihydrite into crystalline products in alkaline media. *Water, Air, and Soil Pollution* **1997,** *97* (3), 397-412.

11. Wang, X.; Li, W.; Harrington, R.; Liu, F.; Parise, J. B.; Feng, X.; Sparks, D. L., Effect of Ferrihydrite Crystallite Size on Phosphate Adsorption Reactivity. *Environmental Science & Technology* **2013,** *47* (18), 10322-10331.

12. Cismasu, A.; Michel, F.; Tcaciuc, A. P.; Brown, G., Properties of impurity-bearing ferrihydrite III. Effects of Si on the structure of 2-line ferrihydrite. *Geochimica et Cosmochimica Acta* **2014,** *133*, 168–185.

13. Vempati, R. K.; Loeppert, R. H., Influence of Structural and Adsorbed Si on the Transformation of Synthetic Ferrihydrite. *Clays and Clay Minerals* **1989,** *37* (3), 273-279.

14. Swedlund, P. J.; Webster, J. G., Adsorption and polymerisation of silicic acid on ferrihydrite, and its effect on arsenic adsorption. *Water Research* **1999,** *33* (16), 3413-3422.

15. Cabello, E.; Morales, M. d. P.; Serna, C.; Barrón, V.; Torrent, J., Magnetic Enhancement During the Crystallization of Ferrihydrite at 25 and 50˚C. *Clays and Clay Minerals - CLAYS CLAY MINER* **2009,** *57*, 46-53.

16. Bolanz, R.; Bläß, U.; Ackermann, S.; Ciobotă, V.; Rösch, P.; Tarcea, N.; Popp, J.; Majzlan, J., The Effect of Antimonate, Arsenate, and Phosphate on the Transformation of Ferrihydrite to Goethite, Hematite, Feroxyhyte, and Tripuhyite. *Clays and Clay Minerals* **2013,** *61*, 11-25.

17. Rzepa, G.; Pieczara, G.; Gaweł, A.; Tomczyk-Chmiel, A.; Zalecki, R., The influence of silicate on transformation pathways of synthetic 2-line ferrihydrite. *Journal of Thermal Analysis and Calorimetry* **2016,** *2016*.

18. Chen, P.; Chen, T.; Xie, Q.; Xu, L.; Liu, H.; Zhou, Y., Mineralogy and Geochemistry of Limonite as a Weathering Product of Ilvaite in the Yeshan Iron Deposit, Tongling, China. *Clays and Clay Minerals* **2018,** *66* (2), 190-207.

19. Putnis, A., Mineral Replacement Reactions. *Reviews in Mineralogy & Geochemistry - REV MINERAL GEOCHEM* **2009,** *70*, 87-124.

20. Schindler, M.; Singer, D. M., Mineral Surface Coatings: Environmental Records at the Nanoscale. *Elements* **2017,** *13* (3), 159-164.

21. Wang, Y.; Bryan, C.; Xu, H.; Gao, H., Nanogeochemistry: Geochemical reactions and mass transfers in nanopores. *Geology* **2003,** *31*.

22. Stubbs, J.; Veblen, L.; Elbert, D.; Zachara, J.; Davis, J.; Veblen, D., Newly recognized hosts for uranium in the Hanford Site vadose zone. *Geochimica et Cosmochimica Acta* **2009,** *73*, 1563-1576.

23. Penn, R. L.; Zhu, C.; Xu, H.; Veblen, D., Iron oxide coatings on sand grains from the Atlantic coastal plain: High-resolution transmission electron microscopy characterization. *Geology* **2001,** *29*.

24. Zhang, S.; Kent, D.; Elbert, D.; Shi, Z.; Davis, J.; Veblen, D., Mineralogy, morphology, and textural relationships in coatings on quartz grains in sediments in a quartz-sand aquifer. *Journal of contaminant hydrology* **2011,** *124*, 57-67.

25. Liu, C.; Shang, J.; Kerisit, S. N.; Zachara, J. M.; Zhu, W., Scale-Dependent Rates of Uranyl Surface Complexation Reaction in Sediments. *Geochimica et Cosmochimica Acta* **2013,** *105*, 326-341.

26. Singer, D. M.; Fox, P. M.; Guo, H.; Marcus, M. A.; Davis, J. A., Sorption and redox reactions of As(III) and As(V) within secondary mineral coatings on aquifer sediment grains. *Environ Sci Technol* **2013,** *47* (20), 11569-76.

27. Schindler, M.; Hochella, M., Soil memory in mineral surface coatings: Environmental processes recorded at the nanoscale. *Geology* **2015,** *43*, 415-418.

28. Schindler, M.; Hochella, M., Nanomineralogy as a new dimension in understanding elusive geochemical processes in soils: The case of low-solubility-index elements. *Geology* **2016,** *44*, G37774.1.

29. Pichler, T.; Veizer, J.; Hall, G. E. M., Natural Input of Arsenic into a Coral-Reef Ecosystem by Hydrothermal Fluids and Its Removal by Fe(III) Oxyhydroxides. *Environmental Science & Technology* **1999,** *33* (9), 1373-1378.

30. Dixit, S.; Hering, J. G., Comparison of Arsenic(V) and Arsenic(III) Sorption onto Iron Oxide Minerals: Implications for Arsenic Mobility. *Environmental Science & Technology* **2003,** *37* (18), 4182-4189.

31. Qi, P.; Pichler, T., Closer Look at As(III) and As(V) Adsorption onto Ferrihydrite under Competitive Conditions. *Langmuir* **2014,** *30* (37), 11110-11116.

32. Waychunas, G. A.; Rea, B. A.; Fuller, C. C.; Davis, J. A., Surface chemistry of ferrihydrite: Part 1. EXAFS studies of the geometry of coprecipitated and adsorbed arsenate. *Geochimica et Cosmochimica Acta* **1993,** *57* (10), 2251-2269.

33. Wang, S.; Zhang, G.; Lin, J.; Wang, X.; Jia, Y., Accurate determination of the As(v) coordination environment at the surface of ferrihydrite using synchrotron extended X-ray absorption fine structure spectroscopy and ab initio Debye–Waller factors. *Environmental Science: Nano* **2019,** *6* (8), 2441-2451.

34. Ehlert, K.; Mikutta, C.; Jin, Y.; Kretzschmar, R., Mineralogical Controls on the Bioaccessibility of Arsenic in Fe(III)–As(V) Coprecipitates. *Environmental Science & Technology* **2018,** *52* (2), 616-627.

35. Fink, J. R., Inda, A.V., Tiecher, T., Barrón, V. , Iron oxides and organic matter on soil phosphorus availability. *Ciência e Agrotecnologia* **2016,** *40*, 369-379.

36. Wang, X.; Hu, Y.; Tang, Y.; Yang, P.; Feng, X.; Xu, W.; Zhu, M., Phosphate and phytate adsorption and precipitation on ferrihydrite surfaces. *Environmental Science: Nano* **2017,** *4* (11), 2193-2204.

37. Wang, L.; Putnis, C.; Ruiz-Agudo, E.; Hövelmann, J.; Putnis, A., In Situ Imaging of Interfacial Precipitation of Phosphate on Goethite. *Environmental science & technology* **2015,** *49*.

38. Pokrovski, G. S.; Schott, J.; Farges, F.; Hazemann, J.-L., Iron (III)-silica interactions in aqueous solution: insights from X-ray absorption fine structure spectroscopy. *Geochimica et Cosmochimica Acta* **2003,** *67* (19), 3559-3573.

39. Schindler, M.; Santosh, M.; Dotto, G.; Silva, L. F. O.; Hochella, M. F., A review on Pb-bearing nanoparticles, particulate matter and colloids released from mining and smelting activities. *Gondwana Research* **2021**.

40. Trivedi, P.; Dyer, J. A.; Sparks, D. L., Lead Sorption onto Ferrihydrite. 1. A Macroscopic and Spectroscopic Assessment. *Environmental Science & Technology* **2003,** *37* (5), 908-914.

41. Dulnee, S.; Banerjee, D.; Merkel, B.; Scheinost, A., Surface Complexation and Oxidation of Sn-II by Nanomagnetite. *Environmental science & technology* **2013,** *47*.

42. Dulnee, S.; Scheinost, A., Surface Reaction of Sn II on Goethite (α-FeOOH): Surface Complexation, Redox Reaction, Reductive Dissolution, and Phase Transformation. *Environmental science & technology* **2014,** *48*.

43. Cismasu, A. C.; Levard, C.; Michel, F. M.; Brown, G. E., Properties of impurity-bearing ferrihydrite II: Insights into the surface structure and composition of pure, Al- and Si-bearing ferrihydrite from Zn(II) sorption experiments and Zn K-edge X-ray absorption spectroscopy. *Geochimica et Cosmochimica Acta* **2013,** *119*, 46-60.

44. Waychunas, G. A.; Fuller, C. C.; Davis, J. A., Surface complexation and precipitate geometry for aqueous Zn(II) sorption on ferrihydrite I: X-ray absorption extended fine structure spectroscopy analysis. *Geochimica et Cosmochimica Acta* **2002,** *66* (7), 1119-1137.

45. Reddy, S. M.; Saxey, D. W.; Rickard, W. D. A.; Fougerouse, D.; Montalvo, S. D.; Verberne, R.; van Riessen, A., Atom Probe Tomography: Development and Application to the Geosciences. *Geostandards and Geoanalytical Research* **2020,** *44* (1), 5-50.

46. Saxey, D.; Moser, D.; Piazolo, S.; Reddy, S.; Valley, J., Atomic worlds: Current state and future of atom probe tomography in geoscience. *Scripta Materialia* **2018,** *148*, 115-121.

47. Devaraj, A.; Perea, D. E.; Liu, J.; Gordon, L. M.; Prosa, T. J.; Parikh, P.; Diercks, D. R.; Meher, S.; Kolli, R. P.; Meng, Y. S., Three-dimensional nanoscale characterisation of materials by atom probe tomography. *International Materials Reviews* **2018,** *63* (2), 68-101.

48. Blum, T. B.; Darling, J. R.; Kelly, T. F.; Larson, D. J.; Moser, D. E.; Perez-Huerta, A.; Prosa, T. J.; Reddy, S. M.; Reinhard, D. A.; Saxey, D. W., Best practices for reporting atom probe analysis of geological materials. *Microstructural Geochronology: Planetary records down to atom scale* **2018**, 369-373.

49. Reddy, S. M.; Saxey, D. W.; Rickard, W. D.; Fougerouse, D.; Montalvo, S. D.; Verberne, R.; Van Riessen, A., Atom probe tomography: development and application to the geosciences. *Geostandards and Geoanalytical Research* **2020,** *44* (1), 5-50.

50. Darling, J. R.; White, L. F.; Kizovski, T.; Černok, A.; Moser, D. E.; Tait, K. T.; Dunlop, J.; Langelier, B.; Douglas, J. O.; Zhao, X.; Franchi, I. A.; Anand, M., The shocking state of apatite and merrillite in shergottite Northwest Africa 5298 and extreme nanoscale chlorine isotope variability revealed by atom probe tomography. *Geochimica et Cosmochimica Acta* **2021,** *293*, 422-437.

51. Branson, O.; Bonnin, E. A.; Perea, D. E.; Spero, H. J.; Zhu, Z.; Winters, M.; Hönisch, B.; Russell, A. D.; Fehrenbacher, J. S.; Gagnon, A. C., Nanometer-scale chemistry of a calcite biomineralization template: Implications for skeletal composition and nucleation. *Proceedings of the National Academy of Sciences* **2016,** *113* (46), 12934-12939.

52. Reinhard, D. A.; Laiginhas, F.; Martens, R. L.; Prosa, T. J., Atom probe tomography (APT) of carbonate minerals. *Micron* **2016**.

53. Pérez-Huerta, A.; Laiginhas, F., Preliminary data on the nanoscale chemical characterization of the inter-crystalline organic matrix of a calcium carbonate biomineral. *Minerals* **2018,** *8* (6), 223.

54. Taylor, S. D.; Liu, J.; Zhang, X.; Arey, B. W.; Kovarik, L.; Schreiber, D. K.; Perea, D. E.; Rosso, K. M., Visualizing the iron atom exchange front in the Fe (II)-catalyzed recrystallization of goethite by atom probe tomography. *Proceedings of the National Academy of Sciences* **2019,** *116* (8), 2866-2874.

55. El Dien, H. G.; Arai, S.; Doucet, L.-S.; Li, Z.-X.; Kil, Y.; Fougerouse, D.; Reddy, S. M.; Saxey, D. W.; Hamdy, M., Cr-spinel records metasomatism not petrogenesis of mantle rocks. *Nature communications* **2019,** *10* (1), 1-12.

56. Genareau, K.; Perez-Huerta, A.; Laiginhas, F., Atom probe tomography analysis of exsolved mineral phases. *JoVE (Journal of Visualized Experiments)* **2019,** (152), e59863.

57. Wu, Y.-F.; Fougerouse, D.; Evans, K.; Reddy, S. M.; Saxey, D. W.; Guagliardo, P.; Li, J.-W., Gold, arsenic, and copper zoning in pyrite: A record of fluid chemistry and growth kinetics. *Geology* **2019,** *47* (7), 641-644.

58. Gopon, P.; Douglas, J. O.; Auger, M. A.; Hansen, L.; Wade, J.; Cline, J. S.; Robb, L. J.; Moody, M. P., A nanoscale investigation of Carlin-type gold deposits: An atom-scale elemental and isotopic perspective. *Economic Geology* **2019,** *114* (6), 1123-1133.

59. Schmidt, J. E.; Ye, X.; van Ravenhorst, I. K.; Oord, R.; Shapiro, D. A.; Yu, Y. S.; Bare, S. R.; Meirer, F.; Poplawsky, J. D.; Weckhuysen, B. M., Probing the location and speciation of elements in zeolites with correlated atom probe tomography and scanning transmission X-ray microscopy. *ChemCatChem* **2019,** *11* (1), 488.

60. Cao, M.; Evans, N. J.; Reddy, S. M.; Fougerouse, D.; Hollings, P.; Saxey, D. W.; McInnes, B. I.; Cooke, D. R.; McDonald, B. J.; Qin, K., Micro-and nano-scale textural and compositional zonation in plagioclase at the Black Mountain porphyry Cu deposit: Implications for magmatic processes. *American Mineralogist: Journal of Earth and Planetary Materials* **2019,** *104* (3), 391-402.

61. White, L. F.; Kizovski, T. V.; Tait, K. T.; Langelier, B.; Gordon, L. M.; Harlov, D.; Norberg, N., Nanoscale chemical characterisation of phase separation, solid state transformation, and recrystallization in feldspar and maskelynite using atom probe tomography. *Contributions to Mineralogy and Petrology* **2018,** *173* (10), 87.

62. Mukherjee, S.; Watanabe, H.; Isheim, D.; Seidman, D. N.; Moutanabbir, O., Laser-assisted field evaporation and three-dimensional atom-by-atom mapping of diamond isotopic homojunctions. *Nano letters* **2016,** *16* (2), 1335-1344.

63. Schirhagl, R.; Raatz, N.; Meijer, J.; Markham, M.; Gerstl, S. S.; Degen, C. L., Nanometer-scale isotope analysis of bulk diamond by atom probe tomography. *Diamond and Related Materials* **2015,** *60*, 60-65.

64. Schindler, M.; Lanteigne, S.; McDonald, A.; Hochella, M., Evidence of CU- and NI-Bearing Surface Precipitates and Adsorption Complexes In Remediated Soils At the Nanoscale: A Tem, Micro-Raman, and Laser-Ablation ICP-MS Study of Mineral Surface Coatings. *The Canadian Mineralogist* **2016,** *54*, 285-309.

65. Shannon, R. D., Revised effective ionic radii and systematic studies of interatomic distances in halides and chalcogenides. *Acta crystallographica section A: crystal physics, diffraction, theoretical and general crystallography* **1976,** *32* (5), 751-767.

66. Philippe, T.; De Geuser, F.; Duguay, S.; Lefebvre, W.; Cojocaru-Mirédin, O.; Da Costa, G.; Blavette, D., Clustering and nearest neighbour distances in atom-probe tomography. *Ultramicroscopy* **2009,** *109* (10), 1304-1309.

67. Philippe, T.; Cojocaru-Mirédin, O.; Duguay, S.; Blavette, D., Clustering and nearest neighbour distances in atom probe tomography: The influence of the interfaces. *Journal of microscopy* **2010,** *239* (1), 72-77.

68. Perea, D. E.; Arslan, I.; Liu, J.; Ristanović, Z.; Kovarik, L.; Arey, B. W.; Lercher, J. A.; Bare, S. R.; Weckhuysen, B. M., Determining the location and nearest neighbours of aluminium in zeolites with atom probe tomography. *Nature communications* **2015,** *6* (1), 1-8.

69. Miller, M.; Forbes, R., *Atom Probe Tomography: The Local Electrode Atom Probe*. 2014.

70. Lanteigne, S.; Schindler, M.; McDonald, A.; Skeries, K.; Abdu, Y.; Mantha, N.; Murayama, M.; Hawthorne, F.; Hochella, M., Mineralogy and Weathering of Smelter-Derived Spherical Particles in Soils: Implications for the Mobility of Ni and Cu in the Surficial Environment. *Water Air and Soil Pollution* **2012,** *223*.

71. Nkongolo, K.; Spiers, G.; Beckett, P.; Narendrula, R.; Theriault, G.; Tran, A.; Kalubi, K., Long-Term Effects of Liming on Soil Chemistry in Stable and Eroded Upland Areas in a Mining Region. *Water, Air, & Soil Pollution* **2012,** *224*.

72. Frueh, A. J., Jr., The crystal structure of claudetite (monoclinic As2O3). *American Mineralogist* **1951,** *36* (11-12), 833-850.

73. Ballirano, P.; Maras, A., Refinement of the crystal structure of arsenolite, As2O3. *Zeitschrift für Kristallographie - New Crystal Structures* **2002,** *217* (2), 177-178.

74. Kitahama, K.; Kiriyama, R.; Baba, Y., Refinement of the crystal structure of scorodite. *Acta Crystallographica Section B* **1975,** *31* (1), 322-324.

75. Dickinson, R. G.; Friauf, J. B., THE CRYSTAL STRUCTURE OF TETRAGONAL LEAD MONOXIDE. *Journal of the American Chemical Society* **1924,** *46* (11), 2457-2463.

76. Hill, R., Refinement of the structure of orthorhombic PbO (massicot) by Rietveld analysis of neutron powder diffraction data. *Acta Crystallographica Section C* **1985,** *41* (9), 1281-1284.

77. Levien, L.; Prewitt, C. T.; Weidner, D. J., Structure and elastic properties of quartz at pressure. *American Mineralogist* **1980,** *65* (9-10), 920-930.

78. Kimmel, A.; Sushko, P.; Shluger, A.; Bersuker, G., Positive and Negative Oxygen Vacancies in Amorphous Silica. *ECS Transactions* **2009,** *19*, 3.

79. Taxer, K.; Bartl, H., On the dimorphy between the variscite and clinovariscite group: Refined finestructural relationship of strengite and clinostrengite, Fe(PO4) · 2H2O. *Crystal Research and Technology* **2004,** *39*, 1080-1088.

80. Baur, W., Uber die Verfeinerung der Kristallstrukturbestimmung einiger Vertreter des Rutiltyps: TiO2, SnO2, GeO2 und MgF2. *Acta Crystallographica* **1956,** *9* (6), 515-520.

81. Smith, K. S., Metal Sorption on Mineral Surfaces: An Overview with Examples Relating to Mineral Deposits. In *The Environmental Geochemistry of Mineral Deposits: Part A: Processes, Techniques, and Health Issues Part B: Case Studies and Research Topics*, Plumlee, G. S.; Logsdon, M. J.; Filipek, L. F., Eds. Society of Economic Geologists: 1997; Vol. 6, p 0.

82. Liu, C.; Liu, Y.; Kerisit, S.; Zachara, J., Pore-Scale Process Coupling and Effective Surface Reaction Rates in Heterogeneous Subsurface Materials. *Reviews in Mineralogy and Geochemistry* **2015,** *80* (1), 191-216.

83. Gagne, O. C.; Hawthorne, F. C., Bond-length distributions for ions bonded to oxygen: results for the non-metals and discussion of lone-pair stereoactivity and the polymerization of PO4. *Acta Crystallographica Section B* **2018,** *74* (1), 79-96.

84. Huminicki, D.; Hawthorne, F., The Crystal Chemistry of the Phosphate Minerals. *Reviews in Mineralogy and Geochemistry* **2002,** *48*, 123-253.

85. Schindler, M.; Hochella, M. F., Sequestration of Pb–Zn–Sb- and As-bearing incidental nanoparticles by mineral surface coatings and mineralized organic matter in soils. *Environmental Science: Processes & Impacts* **2017,** *19* (8), 1016-1027.

86. Mantha, H.; Schindler, M.; Hochella, M. F., Occurrence and formation of incidental metallic Cu and CuS nanoparticles in organic-rich contaminated surface soils in Timmins, Ontario. *Environmental Science: Nano* **2019,** *6* (1), 163-179.

87. Rades, S.; Salge, T.; Schmidt, R.; Hodoroaba, V.-D., Need for Large-Area EDS Detectors for Imaging Nanoparticles in a SEM Operating in Transmission Mode. *Microscopy and Microanalysis* **2014,** *20*, 662-663.

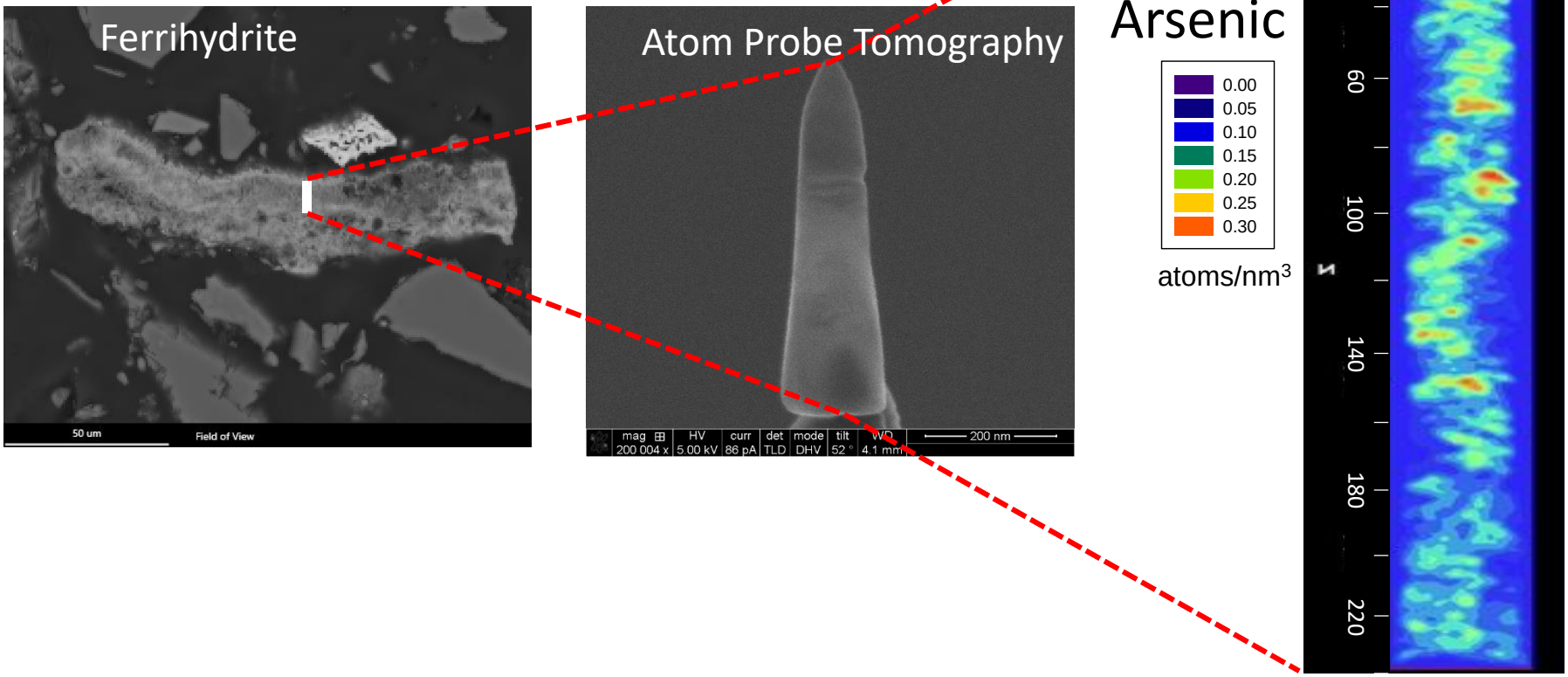
Ferrihydrite
50 um
Field of View
Atom Probe Tomography
mag HV curr det mode tilt WD
200 004 x 5.00 kV 86 pA TLD DHV 52 ° 4.1 mm
200 nm
Arsenic
0.00
0.05
0.10
0.15
0.20
0.25
0.30
atoms/nm3
x
-15
0
15
z
20
60
100
140
180
220